Monthly Notices of the ROYAL ASTRONOMICAL SOCIETY

MNRAS **512,** 6054–6066 (2022) https://doi.org/10.1093/mnras/stac844
Advance Access publication 2022 March 26

A step towards unveiling the nature of three cataclysmic variables: LS Cam, V902 Mon, and SWIFT J0746.3-1608

Nikita Rawat [1,2]★ J. C. Pandey [1]★ Arti Joshi[3] and Umesh Yadava[2]

[1]*Aryabhatta Research Institute of Observational sciencES (ARIES), Nainital 263001, India*
[2]*Deen Dayal Upadhyaya Gorakhpur University, Gorakhpur 273009, India*
[3]*School of Physics and Technology, Wuhan University, Wuhan 430072, China*

Accepted 2022 March 21. Received 2022 February 27; in original form 2021 October 6

ABSTRACT

We have carried out detailed time-resolved timing analyses of three cataclysmic variables (CVs) namely LS Cam, V902 Mon, and SWIFT J0746.3-1608, using the long-baseline, high-cadence optical photometric data from the Transiting Exoplanet Survey Satellite. Our analysis of LS Cam observations hints the presence of a superorbital period of ∼4.025 ± 0.007 d along with negative and positive superhump periods of ∼3.30 and 3.70 h, respectively. These results can be explained as an interaction of nodal and apsidal precession of the accretion disc with orbital motion. For the other two sources, V902 Mon and SWIFT J0746.3-1608, we have found evidence of a beat period of 2387.0 ± 0.6 and 2409.5 ± 0.7 s, respectively, which were not found in earlier studies. Our results presented in this study indicate the change in the accretion mode during the entire observing period for both sources. For V902 Mon, an apparent orbital period derivative of $(6.09 \pm 0.60) \times 10^{-10}$ was also found. Moreover, the second harmonic of orbital frequency dominates the power spectrum of SWIFT J0746.3-1608, suggestive of ellipsoidal modulation of the secondary star. Present analyses suggest that LS Cam could be a superhumping CV, whereas V902 Mon and SWIFT J0746.3-1608 are likely to be variable disc-overflow accreting intermediate polars.

Key words: accretion, accretion discs – stars: individual: (LS Cam; V902 Mon; SWIFT J0746.3-1608) – stars: magnetic field – novae, cataclysmic variables.

1 INTRODUCTION

Cataclysmic variables (CVs) are the semidetached binary systems in which primary is a magnetic white dwarf (WD) that accretes material through a Roche lobe filling late-type main-sequence star, also known as a secondary star. The magnetic field of the WD plays a crucial role in governing the accretion process in these binaries. It also decides two distinct classes of magnetic CVs (MCVs): polars and intermediate polars (IPs). In polars, the magnetic field of the WD is strong enough (typically, in a range of 10–100 MG) to lock the whole system into synchronous (or almost synchronous) rotation. It also prevents the formation of an accretion disc and the accreting material channels directly to the WD magnetic pole(s). While in the case of IPs, magnetic field of the WD is weaker (typically, 1–10 MG) and an accretion disc can form which is disrupted at the magnetospheric radius. Hence, the material from the secondary is accreted either through an accretion stream or an accretion disc or a combination of both. The majority of IPs have spin period of the WD (P_ω), roughly the one-tenth of the orbital period (P_Ω) of the binary system ($P_\omega \sim 0.1\ P_\Omega$) and orbital periods longer than the 'period gap' of 2–3 h (Scaringi et al. 2010). Generally, the higher values of X-ray luminosities of IPs than those of polars is attributed to the higher accretion rate.

The high-energy X-rays originate from the accretion shock and optical emission is seen due to the reprocessing of these X-rays in the surface layers of the disc (including the hotspot) and/or the atmosphere of the secondary. The WD rotation modulates emission in the X-ray and optical regions due to the obscuration by the intervening accretion curtains and reprocessed radiation from axisymmetric parts of the accretion disc. Reprocessing of the beam from parts of the system that rotates with the binary orbital frequency, such as an inflated part of the disc (the hotspot) or the secondary itself, produces an optical beat pulsation. Further, obscurations of the WD by the material rotating in the binary frame and eclipse of the hotspot by an optically thick disc (or ring) give rise to the orbital modulation (Warner 1986, and references therein).

There are primarily three accepted scenarios for accretion in IPs and the feasibility of each one of them depends on the magnetic field strength of WD and mass accretion rate. The first is the disc-fed accretion, in which an accretion disc is present in the system, which is disrupted at the magnetosphere radius. From this radius, material flows along the magnetic field lines resulting in the formation of 'accretion curtains' near the magnetic poles of the WD (Rosen, Mason & Cordova 1988). The second is the disc-less or stream-fed accretion, in which the high magnetic field of the WD does not allow the formation of a disc and infalling material is channelized along the magnetic field lines to the pole caps (Hameury, King & Lasota 1986). In the third possibility, known as disc-overflow accretion (Lubow 1989; Armitage & Livio 1996), disc-fed and stream-fed accretions can simultaneously occur as a part of the accretion stream skims over the disc and then interacts with the magnetosphere of the WD (Hellier et al. 1989; King & Lasota 1991). In all these accretion scenarios, whenever accretion takes place via a disc, the accreting

★ E-mail: nikita@aries.res.in (NR); jeewan@aries.res.in (JCP)

material impacts on to both magnetic poles and whenever accretion takes place via a stream, accretion occurs at both poles continuously with varying accretion rate and only a fraction of accretion flow flips between two poles.

A featured characteristic of IPs is the presence of multiple periodicities in the X-ray and optical power spectra because of the complex interactions between the spin and orbital modulations. Therefore, the presence of spin, beat, orbital, and other sideband frequencies in the power spectra and their amplitudes play a vital role in distinguishing the mode of accretion in the system. In the disc-fed accretion, modulation at the spin frequency (ω) of the WD occurs (Kim & Beuermann 1995; Norton, Beardmore & Taylor 1996), whereas stream-fed accretion gives rise to modulation at the lower orbital sideband of the spin frequency, i.e. beat (ω - Ω) frequency (Hellier 1991; Wynn & King 1992). Wynn & King (1992) also showed that if there is an asymmetry between the magnetic poles, stream-fed accretion can also produce a modulation at the spin frequency, in addition to that at the beat frequency. Hence, 2ω - Ω frequency plays an important role in distinguishing between these two modes of accretion in X-ray bands and only present in discless systems along with sometimes dominant Ω component, ω - Ω, and ω. For a disc-overflow accretion, where disc-fed and stream-fed simultaneously occur, modulations at both ω and ω - Ω frequencies are expected to occur (see Hellier 1991, 1993). Further, the variable nature of accretion flow is one of the basic characteristics of an IP and has been observed in IPs e.g. TX Col and FO Aqr for a number of times (see Norton et al. 1992, 1997; Hellier 1993; Beardmore et al. 1996; Wheatley 1999; Littlefield et al. 2020; Rawat, Pandey & Joshi 2021, for details).

In this paper, we present a detailed investigation of three CVs namely LS Cam, V902 Mon, and SWIFT J0746.3-1608, based on their high-cadence long-baseline Transiting Exoplanet Survey Satellite (TESS) observations. These sources are taken from the IP catalogue of Koji Mukai.[1] Our aim is to explore the true nature of all three sources.

The paper is structured as follows. Section 2 reviews each of the sources individually and in Section 3, we describe observations and data used for this study. Sections 4, 5, and 6 contains our analysis and results for LS Cam, V902 Mon, and J0746, respectively. Finally, discussion and summary are presented in Sections 7 and 8, respectively.

2 REVIEW OF SOURCES

2.1 LS Cam

LS Cam (HS 0551 + 7241) was discovered as a CV by Dobrzycka et al. (1998) using spectroscopic observations. It is located at a distance of $1.7^{+0.1}_{-0.1}$ kpc (Gaia Collaboration 2021). The identification spectrum of LS Cam, obtained in 1995, revealed features typical for a CV: H I, He II, and He I emission lines on the top of a blue continuum. The periodogram analysis of the Hα, Hβ, and He II λ4686 radial velocities revealed that the hydrogen lines are likely dominated by the S-wave component, following the orbital variations with a period of 4 h. At the same time, He II λ4686 line shows rapid fluctuations of $\sim$50 min. So, based on these variations, Dobrzycka et al. (1998) concluded that LS Cam might be an IP. Additionally, from the analysis of emission-line radial velocity curves, Thorstensen et al. (2017) confirmed the orbital period of LS Cam to be 3.417 h.

[1]http://asd.gsfc.nasa.gov/Koji.Mukai/iphome/iphome.html

2.2 V902 Mon

The source V902 Mon was identified as a CV in the Isaac Newton Telescope Photometric Hα Survey of the northern Galactic plane (IPHAS) survey due to its prominent Hα emission (Witham et al. 2007). Using the optical photometric observations, Aungwerojwit et al. (2012) classified it as a deeply eclipsing IP with an orbital period of 8.162 h and spin period of WD of $\sim$2210 s. Further, the spin modulation was found to be varying in their observing runs between 2006 and 2009, sometimes too weak to be noticeable. However, between 2008 and 2017, Worpel et al. (2018) found the spin period of 2208 s at multiple epochs and concluded that V902 Mon accretes via disc only due to the absence of beat modulations. The distance of V902 Mon is found to be $3.1^{+0.8}_{-0.5}$ kpc (Gaia Collaboration 2021).

2.3 SWIFT J0746.3-1608

SWIFT J0746.3-1608 (hereafter J0746) was discovered in the Swift/BAT survey and found to be a highly variable X-ray source at a distance of 625^{+10}_{-8} pc (Gaia Collaboration 2021). From optical observations, Thorstensen & Halpern (2013) found an orbital period of 9.38 h and reported that J0746 might belong to the class of either Nova-like variable or an IP. Bernardini et al. (2019) concluded that J0746 might be an IP with a plausible spin period of $\sim$2300 s. However, due to the short X-ray coverage, they could not separate this periodicity from the beat and other sidebands most commonly found in the power spectra of IPs. From comparative studies of *XMM–Newton* observations of 2016 and 2018, they also confirmed that J0746 has returned to its high state in 2018.

3 OBSERVATIONS AND DATA

We have used the archival data from TESS for all three sources. The TESS instrument consists of four wide-field CCD cameras, each with field of view of 24° × 24° so that all cameras can image a region of the sky measuring 24° × 96°. TESS observations are broken up into sectors, each lasting two orbits, or about 27.4 d and conducts its downlink of data while at perigee. This results in a small gap in the data compared to the overall run length. The TESS bandpass extends from 600 to 1000 nm with an effective wavelength of 800 nm (see Ricker et al. 2015, for details). The log of observations for each source is given in Table 1. The data were stored in Mikulski Archive for Space Telescopes data archive[2] with unique identification numbers 'TIC 138042556', 'TIC 334061567', and 'TIC 234712743', for LS Cam, V902 Mon, and J0746, respectively. The cadence for each source was 2 min; however, for J0746 the data were available at a cadence of 20 s also. For our analysis, we have taken 'PDCSAP' flux, which is the simple aperture photometry (SAP) flux after removing the common instrumental systematics from it using the co-trending basis vectors. The PDCSAP flux also corrects for the amount of flux captured by the photometric aperture and crowding from known nearby stars.[3] The data taken during an anomalous event had quality flags greater than 0 in the FITS file data structure, and thus we have considered only the data with the 'quality flag' = 0.

Wherever available, we have also used the Zwicky Transient Facility (ZTF[4], Bellm et al. 2019) r and g bands data and American

[2]https://mast.stsci.edu/portal/Mashup/Clients/Mast/Portal.html
[3]See Section 2.0 of the TESS Archive Manual at https://outerspace.stsci.edu/display/TESS/2.0+-+Data+Product + Overview
[4]https://www.ztf.caltech.edu/

Table 1. Observation log of sources where start and end time are in calendar date.

Source name	Sector	Start time	End time	Total observing days
LS Cam	19	2019-11-28T14:04:20.676	2019-12-23T15:26:46.080	24.8
	20	2019-12-25TT00:08:45.948	2020-01-20T07:48:03.141	26.3
	26	2020-06-09T18:17:54.123	2020-07-04T15:07:55.466	24.9
	40	2021-06-25T03:33:33.297	2021-07-23T08:24:18.088	28.2
V902 Mon	33	2020-12-18T05:40:40.133	2021-01-13T01:50:30.998	25.8
SWIFT J0746.3-1608	34	2021-01-14T06:29:41.446	2021-02-08T13:39:28.238	25.0

Association of Variable Star Observers (AAVSO[5], Kafka 2021) CV (Clear or unfiltered reduced to V sequence), V (Johnson V), and I (Johnson I) bands data to represent the long-term behaviour of sources. The ground-based data are available only for the source LS Cam and V902 Mon. We found a positive linear dependence of TESS magnitude on the simultaneous ground-based magnitudes, which indicates that PDCSAP flux values appear to be following the flux observed from ground-based observations. None the less, as noted in the TESS archival manual[6] and also pointed out by Littlefield et al. (2021) that in the PDCSAP data, the periodic variability should be unaffected but slow, aperiodic variability (such as that from a low-amplitude outburst) might be removed. Thus, the results presented in this manuscript can be taken with caution if aperiodic variabilities such as quasi-periodic oscillations have been removed from PDCSAP flux values after processing from SAP flux values.

4 LS CAM

4.1 Light curve and power spectral analysis

Fig. 1(a) shows the long-term light curve of LS Cam, where the variable nature of the source is visible. The average change in magnitude in the AAVSO-CV band is in the range ∼16.6–15.7 and on some occasions, it has gone to a fainter state with a magnitude more than 17.3. To overplot the TESS light curve, we have converted TESS flux unit of electrons per second to magnitude using the zero-point value of 20.44 (Vanderspek et al. 2018; Fausnaugh et al. 2021). The inset of Fig. 1(a) shows some of the simultaneous observations between ZTF-r and TESS, which confirms that during these observations, LS Cam was always in a relatively stable high state. Fig. 1(b) shows the TESS light curve of LS Cam. There is a gap of almost 5 months between the observations in sectors 20 and 26 and a gap of 1 yr between sectors 26 and 40. Further, sector 26 has a mean flux value of 26.22 ± 0.08 e^{-}/s compared to the mean flux value of 40.70 ± 0.05 e^{-}/s, 46.92 ± 0.07 e^{-}/s, and 66.87 ± 0.05 e^{-}/s of the sectors 19, 20, and 40, respectively. Unfortunately, there were no simultaneous observations corresponding to sector 26 observations, but similar low states were also seen during the previous observations corresponding to BJDs 2456580.39, 2457718.29, and 2458353.99. This may indicate that that there might have been a change in the system's state during the sector 26 observations.

To find the periodic signals in the data, we have performed the Lomb–Scargle (LS) periodogram analysis (Lomb 1976; Scargle 1982). The LS power spectrum of all four sectors is shown in Fig. 2. Several peaks are present in the power spectrum of LS Cam. The significance of these detected peaks is determined by calculating the false-alarm probability (Horne & Baliunas 1986). The horizontal dashed line in each power spectrum represents the 90 per cent confidence level. The derived periods from the periodogram analyses are given in Table 2. The periods corresponding to four dominant peaks from the combined data of all sectors are 4.025 ± 0.007 d, 3.4171 ± 0.0002 h, 3.3007 ± 0.0002 h, and 1.67896 ± 0.00005 h.

The 3.417 h periodicity is identified as the orbital period of the system. For the orbital phase folding the data, we have taken the 1-d time-resolved data segments to see the short-term variations. The reference time for folding was taken to be the observation starting time as extremums could not be adequately identified in the light curve. Each light curve was folded with the binning of 20 points in a phase. We have shown the orbital phase-folded profile in Fig. 3. The top two panels correspond to the observations of sectors 19 and 20, whereas the bottom two panels correspond to the observations of sectors 26 and 40, respectively. The orbital modulation was found to be highest in sector 26, lowest in sector 40, and intermediate in sectors 19 and 20. In all sectors, a ∼4-d periodic variation in all orbital phase-folded profiles seems to be taking place.

Other frequencies identified in power spectral analyses can be explained based on the following two scenarios.

4.1.1 Scenario A

In this scenario, if we consider 1.67896 h as spin period (P_ω) of WD, the beat period ($P_{\omega-\Omega} = \frac{P_\Omega P_\omega}{P_\Omega - P_\omega}$) is estimated to be 3.30 h, which is present in all four sectors' observation. Considering these values of orbital, spin, and beat periods, the periods corresponding to various harmonics $\omega - 2\Omega$, 2Ω, $2(\omega - \Omega)$, $3(\omega - \Omega)$, $2\omega - \Omega$, and $2\omega - 3\Omega$ should be 4.025 d, 1.71 h, 1.65 h, 1.10 h, 1.11h, and 3.19 h, respectively, which are present in the power spectrum of LS Cam. The presence of all these frequencies speculates that LS Cam can be an IP. However, as $\omega + \Omega$ was not found to be present in the power spectrum, the maximum value of the amplitude of $\omega - 2\Omega$ allowed by the model for optical power spectra of IPs predicted by Warner (1986) should be half of that of $\omega - \Omega$, which was also found for V1223 Sgr by Warner & Cropper (1984). For LS Cam, $\omega - 2\Omega$ was the largest-amplitude signal in all sectors, which weakens its possibility of being an IP based on the above-identified frequencies. Further, if considered all frequencies belong to an IP class for LS Cam then we have no explanation for the origin of ∼3.7 h periodicity in sectors 26 and 40.

4.1.2 Scenario B

Considering the orbital period (P_{ω_o}) of the system as 3.41 h, the periodicity of 3.30 h can be a negative superhump (P_{ω_-}) because it has slightly less period than the P_{ω_o}. Thus, the 4.025 d period could be the superorbital period (P_N). In this assumption, the periods of 3.19 h, 1.71 h, 1.68 h, 1.65 h, 1.11 h, 1.10 h can be designated as P_{ω_o+2N}, $P_{2\omega_o}$, $P_{2\omega_o+N}$, $P_{2\omega_-}$, $P_{3\omega_o+2N}$, and $P_{3\omega_-}$, respectively. There are

[5]https://www.aavso.org/

[6]See Section 2.1 of the TESS Archive Manual at https://outerspace.stsci.edu/display/TESS/2.1+Levels+of+data + processing

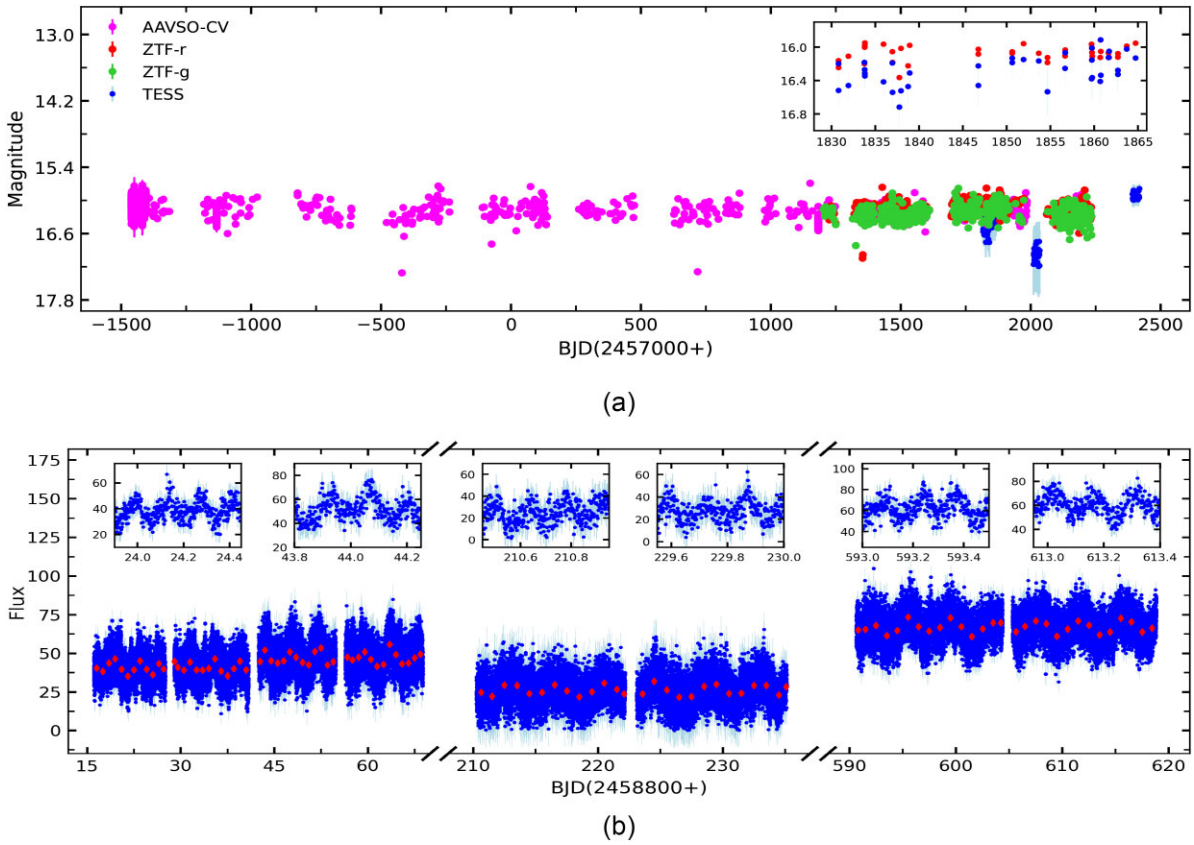

Figure 1. (a) Long-term variable light curve of LS Cam as observed from AAVSO, ZTF, and TESS. Inset of the figure shows the simultaneous observations from TESS and ZTF-r. (b) TESS light curve of LS Cam of the sectors 19, 20, 26, and 40, where the red diamonds represent the mean flux of each day. Inset of the figure shows close-up of some variability cycles.

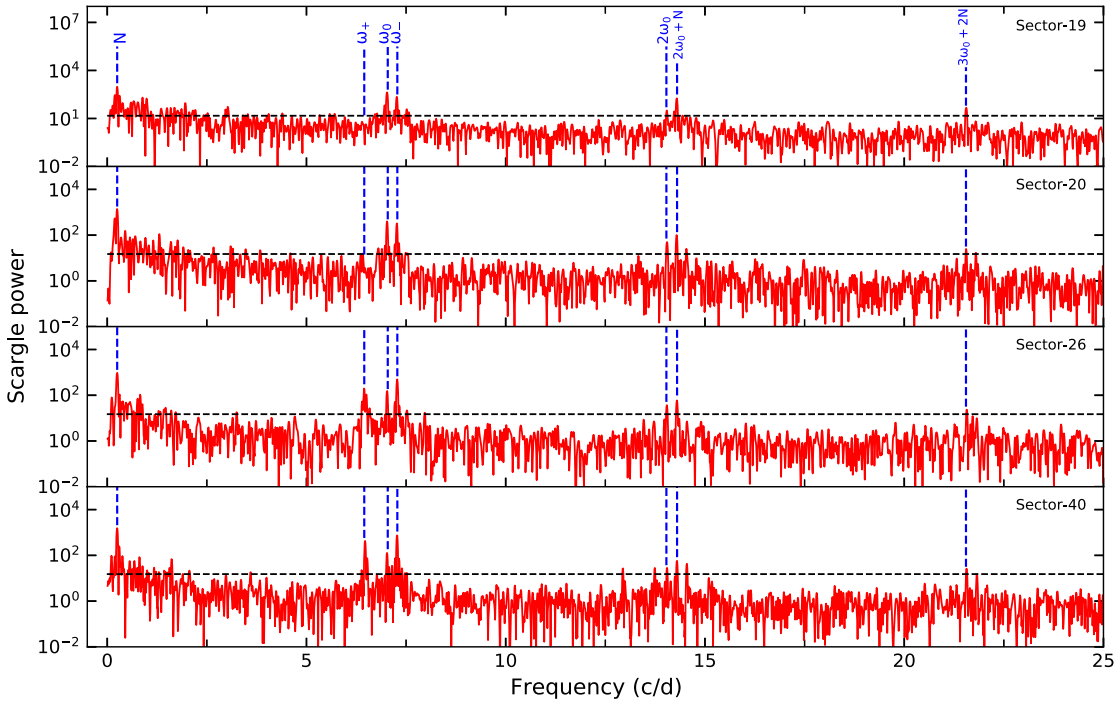

Figure 2. Power spectra of LS Cam of all sectors. Major frequencies are marked for clear visual inspection.

Table 2. Periods corresponding to the dominant frequency peaks in the power spectra of LS Cam of the observations of all four sectors.

Identification	Period (d*/h)				
	Sector 19	Sector 20	Sector 26	Sector 40	Combined
$P_N^a/P_{\omega-2\Omega}{}^b$	3.97 ± 0.16*	4.05 ± 0.16*	3.98 ± 0.16*	4.03 ± 0.14*	4.025 ± 0.007*
$P_{\omega_o}{}^a/P_{\Omega}{}^b$	3.416 ± 0.005	3.419 ± 0.005	3.415 ± 0.005	3.418 ± 0.004	3.4171 ± 0.0002
$P_{\omega_-}{}^a/P_{\omega-\Omega}{}^b$	3.302 ± 0.004	3.303 ± 0.004	3.297 ± 0.004	3.302 ± 0.004	3.3007 ± 0.0002
$P_{\omega_+}{}^a$	–	–	3.724 ± 0.006	3.709 ± 0.005	–
$P_{2\omega_o+N}{}^a/P_{\omega}{}^b$	1.679 ± 0.001	1.680 ± 0.001	1.679 ± 0.001	1.678 ± 0.001	1.67896 ± 0.00005
$P_{2\omega_o}{}^a/P_{2\Omega}{}^b$	1.709 ± 0.001	1.708 ± 0.001	1.709 ± 0.001	1.708 ± 0.001	1.70860 ± 0.00005
$P_{3\omega_o+2N}{}^a/P_{2\omega-\Omega}{}^b$	1.1132 ± 0.0005	1.1135 ± 0.0005	1.1129 ± 0.0005	1.1132 ± 0.0005	1.11316 ± 0.00002
$P_{\omega_o+2N}{}^a/P_{2\omega-3\Omega}{}^b$	3.192 ± 0.004	3.202 ± 0.004	3.191 ± 0.004	3.193 ± 0.004	–
$P_{2\omega_-}{}^a/P_{2(\omega-\Omega)}{}^b$	–	1.651 ± 0.001	–	1.650 ± 0.001	–
$P_{3\omega_-}{}^a/P_{3(\omega-\Omega)}{}^b$	–	1.1009 ± 0.0005	–	1.0996 ± 0.0004	–

Notes. [a]Identification of periods based on scenario B.
[b]Identification of periods based on scenario A. Please see Sections 4.1.1 and 4.1.2 for details.

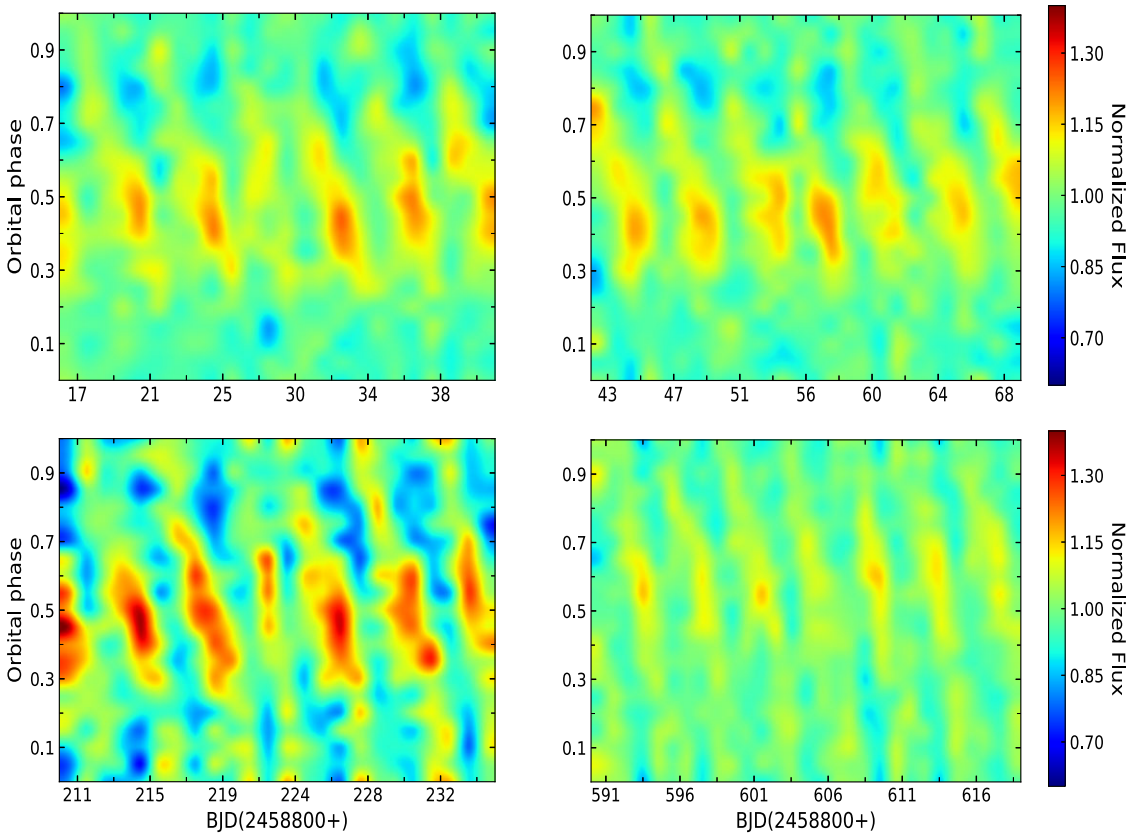

Figure 3. Phase-folded light curves of LS Cam for orbital period. The top two panels correspond to sectors 19 and 20, whereas the bottom two panels correspond to sectors 26 and 40, respectively. The colourbars (normalized flux) have been used for representing the modulations.

mainly two possibilities for the presence of several days superorbital period in CVs. The first one is due to the 'short outbursts' of ER UMa-type dwarf novae (see Robertson, Honeycutt & Turner 1995, for details). Since no outbursts have been detected for LS Cam, the superorbital period found here cannot be attributed to the outbursts of ER UMa-type dwarf novae. However, superorbital period in CVs is also associated with retrograde precession of an accretion disc (see Patterson et al. 1997, for details). Generally, these systems satisfy the relation $\omega_o + N = \omega_-$, where ω_- corresponds to the frequency of a 'negative superhump'. In this way, a period slightly more than the P_{ω_o} is known as the positive superhump period (P_{ω_+}) which in turn indicates that the ∼3.7 h period in sectors 26 and 40 is P_{ω_+} . The origin of P_{ω_+} in CVs is thought to be due to the prograde precession of the lines of apsides of an eccentric disc (Whitehurst 1988; Osaki 1989; Lubow 1991), while P_{ω_-} arises due to the retrograde precession of the line of nodes of a disc that has tilted out of the orbital plane (Harvey et al. 1995; Patterson et al. 1997; Wood, Montgomery & Simpson 2000; Murray et al. 2002). The superorbital period found in the TESS power spectra of LS Cam could be associated with the retrograde precession of the disc, as we have not found the precession period associated with prograde precession, which should be around ∼1.8 d. Since this scenario explains all the frequencies present in the

power spectra more appropriately than that of scenario A, for further discussion, we have considered LS Cam as a superhumping CV.

The positive period excess parameter ϵ_+ with positive superhump and orbital period is related by $\epsilon_+ = (P_{\omega_+} - P_{\omega_o})/P_{\omega_o}$. For the negative superhump period, this relation modifies as $\epsilon_- = (P_{\omega_-} - P_{\omega_o})/P_{\omega_o}$ to define the negative superhump period deficit. The value of ϵ_+ in sectors 26 and 40 was derived to be 0.090 ± 0.002 and 0.085 ± 0.002, respectively. We have taken an average value of 0.0875 ± 0.0035 for our further calculations. With this large value of ϵ_+, LS Cam joins BB Dor, which has the largest value of ϵ_+ of ∼0.09 (Patterson et al. 2005). However, the value of ϵ_- in sectors 19, 20, 26, and 40 was calculated to be −0.033 ± 0.002, −0.034 ± 0.002, −0.034 ± 0.002, and −0.034 ± 0.002, and these values are well consistent with each other. Therefore, using the values of periods obtained from the combined data, ϵ_- was calculated to be −0.03406 ± 0.00008. Therefore, the ratio of period excess to period deficit ($\phi = \epsilon_-/\epsilon_+$) for LS Cam was found to be ∼−0.39. The similar value for ϕ has also been found for TT Ari (−0.40) and TV Col (−0.36) (see table 2 of Retter et al. 2002). The superhump excess has been shown to be correlated with the mass ratio ($q = M_2/M_1$) of the binary system components by Patterson et al. (2005) with the relation: $\epsilon_+ = 0.18q + 0.29q^2$. However, this relation suffers from the difficulty of not considering pressure effect within the accretion disc as suggested by Kato (2022). Using the above-mentioned relation of Patterson et al. (2005), the value of q was thus estimated to be ∼0.32. Using the mean empirical linear mass–period relation of Smith & Dhillon (1998), M_2 was estimated to be ∼0.32 M⊙. Using above-mentioned values of q and M_2, the mass of WD was estimated to be ∼1.0 M⊙ for LS Cam.

5 V902 MON

5.1 Light curve and power spectral analysis

The long-term light curve of V902 Mon is shown in Fig. 4(a), for which we have used data from AAVSO-CV, AAVSO-V, AAVSO-I, ZTF-r, and ZTF-g. The shaded region in the figure corresponds to the TESS observations. Fig. 4(b) shows the entire TESS light curve along with some of the simultaneous data points between AAVSO and TESS. We have performed LS periodogram analysis to find the periodicities in the data, and the corresponding power spectrum is presented in Fig. 5(a), where we have marked the positions of all the identified frequencies. These frequencies are Ω, 2Ω, 3Ω, 4Ω, 5Ω, 6Ω, 7Ω, 8Ω, 9Ω, 10Ω, 11Ω, ω - 2Ω , ω - Ω , and ω . All frequencies except 4Ω, 5Ω, and 6Ω are above the 90 per cent significance level, which is denoted with the black dotted line in the power spectrum. The periods corresponding to all these frequencies are given in Table 3. We found an orbital period of 8.16 ± 0.03 h and a spin period of 2207.6 ± 0.5 s, confirming the previous results of Aungwerojwit et al. (2012) and Worpel et al. (2018). In contrast to earlier epochs, a period of 2387.0 ± 0.6 s was found in the power spectra, which we assign as the beat period of the system. The power at spin frequency was found to be higher than the power at the beat frequency in the power spectrum. In addition to that, a period of 2599.7 ± 0.8 s was also present, which corresponds to the lower orbital sideband of beat frequency (ω - 2Ω). The simultaneous presence of ω - 2Ω along with the ω - Ω frequency confirms the origin of ω - 2Ω to be the orbital modulation of the ω - Ω component, as pointed by Warner (1986). In addition to this, the orbital modulation of the ω - Ω component also changes the power at ω frequency because ω - Ω ± Ω = ω - 2Ω and ω . Further, the absence of ω + Ω frequency also suggests that the origin of ω - Ω cannot be the orbital modulation of ω component; otherwise, both orbital modulations of ω frequency (ω - Ω and ω + Ω) should have been present in the power spectrum. The ω - 2Ω frequency can also originate from the modulation of ω at half the orbital period, but we did not find the presence of ω + 2Ω in the power spectrum. Therefore, the presence of ω and ω - Ω frequencies along with the ω - 2Ω component in the combined power spectrum obtained from the analysis of TESS observations of late 2020 show that V902 Mon accretes via a combination of disc and stream with a dominance of disc-fed accretion.

5.2 Ephemeris and O-C analysis

Intending to refine the previous ephemeris, we have calculated eclipse mid-points by fitting the eclipses with a constant plus a Gaussian. We found 71 timings of minima from TESS and 21 timings of minima from AAVSO where five of them were simultaneous. The newly derived times of minima are given in Table 4, where errors are given in parenthesis. We converted minima timings from AAVSO and earlier reported timings by Witham et al. (2007) and Aungwerojwit et al. (2012) to BJD using the algorithm of Eastman, Siverd & Gaudi (2010). We then combined the timings of the eclipse minima from our data with the previous timings of Witham et al. (2007), Aungwerojwit et al. (2012), and Worpel et al. (2018). We have taken the uncertainties for previously reported timings as described in Worpel et al. (2018). A linear fit between the cycle numbers and minima timings provided the following ephemeris for V902 Mon:

$$T_0 = 2453340.4944(9) + 0.34008396(6) \times E, \quad (1)$$

where T_0 is defined as the time of mid-eclipse and the errors are given in parenthesis.

From equation (1), we refined the orbital period to be 8.162015 ± 0.000002 h. Observed minus calculated (O-C) to the eclipse timings fit are shown in Fig. 6 and a clear trend is visible, suggesting a period change in V902 Mon. By fitting a parabola between O-C and cycle numbers, the apparent orbital period derivative was found to be (6.09 ± 0.60) × 10^{-10}.

5.3 Time-resolved power spectra and phase-folded light curves

We have also explored the time-resolved power spectral analysis for V902 Mon. Fig. 5(b) shows the power spectrum with a time binning of 1 d. The bottom panel of Fig. 5(b) shows a change in the power of the orbital frequency. However, the top panel represents the power spectrum obtained after removing the data points corresponding to the eclipse region so that the orbital modulation effect can be ignored. As visible from the figure, the 1-d time-resolved power spectrum shows the change in the powers of Ω , ω , ω - Ω , and ω - 2Ω frequencies with Ω frequency being dominant. The ω - Ω frequency was not detected for 7 d in the power spectra, indicating that V902 Mon is probably accreting predominantly through the disc. For the rest 18 d, both ω and ω - Ω frequencies were present in the power spectra with varying dominance speculating a disc-overflow system on these days. Out of these 18 d, the system was found to be the disc-overflow accretor with disc-fed dominance on 11 d and stream-fed dominance on 7 d. Interestingly, it was found that during Days 4 and 7 to 13, ω - 2Ω was present in the power spectrum and on those days ω - Ω was not strong enough such that its orbital modulation can originate a strong power at ω - 2Ω . Therefore, the origin of ω - 2Ω during these days can be considered the modulation of ω at half the orbital period. A weak ω + 2Ω was also found to be present during these days. The simultaneous presence of ω - 2Ω and ω + 2Ω with unequal amplitudes was also seen in EX Hya by Siegel

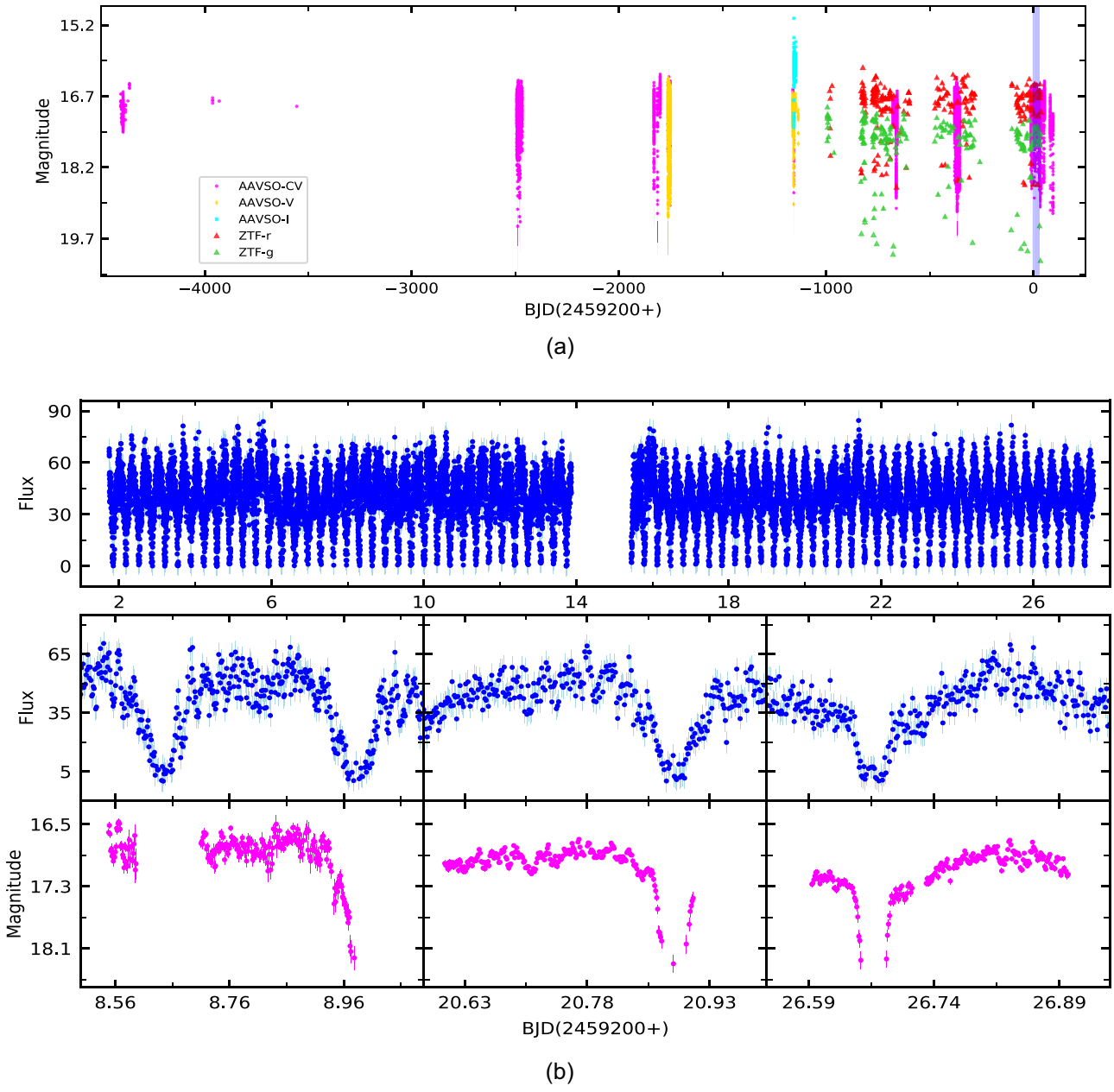

Figure 4. (a) Long-term variable light curve of V902 Mon, where the shaded region corresponds to the TESS observations. (b) Top panel: TESS light curve of V902 Mon. The middle and bottom panels show some of the simultaneous observations between TESS and AAVSO.

et al. (1989). Moreover, if we compare our results with previous studies of Aungwerojwit et al. (2012) and Worpel et al. (2018), we can say that those observations might have occurred during those times when accretion through the stream was not significant enough to provide a beat modulation.

One-day time-resolved data segments were also taken for folding over orbital, spin, and beat periods using the updated ephemeris described in equation (1). The left panel of Fig. 7 shows the orbital phase-folded light curve of V902 Mon. The out of the eclipse flux value was ∼65 e^{-}/s, which dropped to ∼0 e^{-}/s, suggesting the nature of the eclipse to be total. The eclipse phase-width was found to be almost constant during the entire observing period, which was quantified by measuring the total duration of ingress to egress in these 1-d folded light curves. The region between phases 0.88 and 1.07 in the orbital folded light curve in the left panel of Fig. 7 represents this. The data were also folded over spin and beat periods after removing the eclipse region from each data set. The middle and right panels of Fig. 7 represent the colour composite plots for spin and beat folded light curves, respectively. The interplay between the dominance of spin modulation and beat modulation is observed, which is consistent with the time-resolved power spectrum.

TESS observations of V902 Mon unveils the dynamic behaviour of its accretion geometry from pure disc-fed to variable disc-overflow. We have checked the ground-based data for V902 Mon for the epoch of TESS observations. Similar to Aungwerojwit et al. (2012), we have considered the out-of-eclipse brightness variations by measuring the average magnitude in the phase interval 0.78–0.88 and 1.1–1.2. It was found that during TESS observations, the

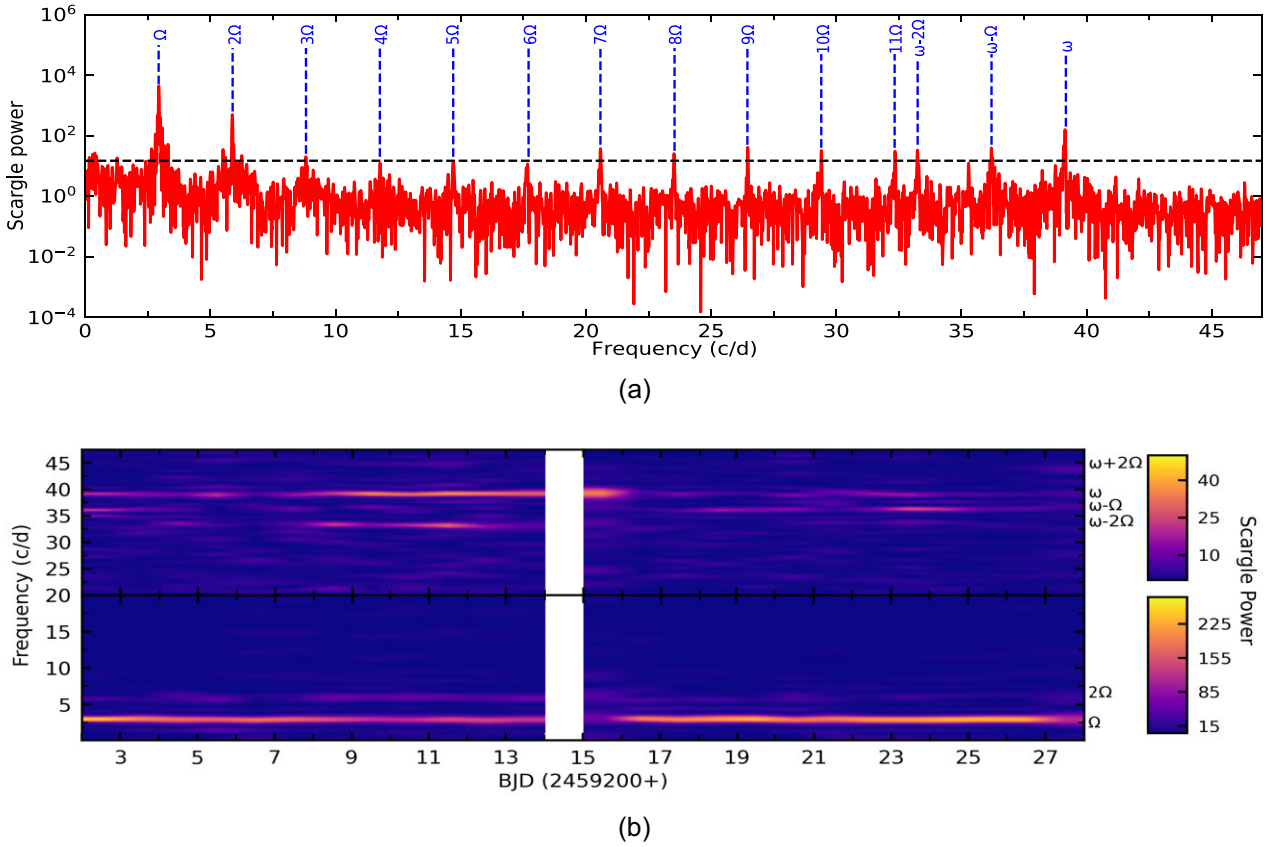

Figure 5. (a) Power spectrum of V902 Mon, where the major frequencies are marked for clear visual inspection. (b) Time-resolved power spectrum of V902 Mon with a time-bin of 1 d.

Table 3. Periods corresponding to the dominant peaks in the power spectrum of V902 Mon.

Identification	Period
P_{Ω} (h)	8.16 ± 0.03
P_{ω} (s)	2207.6 ± 0.5
$P_{\omega-\Omega}$ (s)	2387.0 ± 0.6
$P_{2\Omega}$ (h)	4.086 ± 0.007
$P_{3\Omega}$ (h)	2.723 ± 0.003
$P_{7\Omega}$ (h)	1.1662 ± 0.0006
$P_{8\Omega}$ (h)	1.0204 ± 0.0004
$P_{9\Omega}$ (h)	0.9070 ± 0.0003
$P_{10\Omega}$ (h)	0.8162 ± 0.0003
$P_{11\Omega}$ (h)	0.7420 ± 0.0002
$P_{\omega-2\Omega}$(s)	2599.7 ± 0.8

out-of-eclipse magnitude of V902 Mon varies by ∼0.5 mag. We have found a negative correlation of −0.8 with a null hypothesis probability of 0.027 between AAVSO magnitude and spin amplitude. We also calculated the average TESS flux in the above-mentioned phases and found a positive correlation of 0.6 with a null hypothesis probability of 0.002 between flux and spin amplitude. This suggests that during faint states, the contribution from the disc decreases, thus resulting in a lower value of spin modulation. However, we did not find a significant correlation between TESS flux and beat amplitude with a correlation value of −0.35 and a null hypothesis probability of 0.092. In previous studies by Norton et al. (1997) and Littlefield et al. (2020), a change in the mass accretion rate is typically considered the reason behind changing accretion mode in IPs. However, there are two other possibilities given by Norton et al. (1997): the behaviour of companion star and changes in the disc itself.

5.4 Nature of eclipse profiles

To inspect whether spin pulse impacts the profile of the eclipses as seen in a previous study of Aungwerojwit et al. (2012), we have probed the morphology of eclipse profiles. They argued that the spin amplitude was weaker with box-shaped eclipse profiles and higher with round-shaped eclipse profiles. They also found that the eclipse depth was more in box-shaped profiles than the round-shaped profiles. Moreover, Worpel et al. (2018) also found a similar result with the magnitude near the eclipse mid-point of 19.0 in flat bottom profiles rather than 18.5 in the round-shaped profile.

We have also explored all these scenarios using current data. All eclipse profiles were inspected visually wherever the data were rich enough to give a clear identification. Using AAVSO-CV data, two flat profiles with magnitudes near eclipse mid-point of 18.6 and 18.9, and seven round profiles with magnitudes in the range of 18.3–18.7 were found. We did not notice any clear-cut hallmark to identify the eclipse profile by measuring the mid-point brightness of the eclipse. Further, the eclipse depth for two flat profiles were 1.3 and 1.7 mag, whereas, for round profiles, it has a range of 1.2–1.5 mag. Therefore, the high value of eclipse depth does not clearly imply that it would have flat bases. The power spectra of the AAVSO observations corresponding to round-shaped eclipse profiles show either presence or dominance of spin frequency, whereas flat-shaped eclipse profiles have either only beat or beat dominance.

Table 4. Eclipse mid-points for V902 Mon from recent observations from TESS and AAVSO.

Eclipse mid-point (BJD)	Cycle	Eclipse mid-point (BJD)	Cycle	Eclipse mid-point (BJD)	Cycle	Eclipse mid-point (BJD)	Cycle
2458538.6779(2)	15 285	2459205.581(1)	17 246	2459213.404(1)	17 269	2459222.5863(9)	17 296
2458825.0301(4)	16 127	2459205.924(1)	17 247	2459213.743(1)	17 270	2459222.928(1)	17 297
2458829.1108(5)	16 139	2459206.266(2)	17 248	2459215.783(1)	17 276	2459223.269(1)	17 298
2458832.1709(4)	16 148	2459206.604(2)	17 249	2459216.128(1)	17 277	2459223.607(1)	17 299
2458834.2104(4)	16 154	2459206.945(1)	17 250	2459216.467(2)	17 278	2459223.9473(9)	17 300
2458842.0353(8)	16 177	2459207.285(1)	17 251	2459216.807(1)	17 279	2459224.2865(9)	17 301
2458843.0530(4)	16 180	2459207.625(2)	17 252	2459217.148(2)	17 280	2459224.627(1)	17 302
2458844.0728(3)	16 183	2459207.962(2)	17 253	2459217.488(2)	17 281	2459224.9689(9)	17 303
2459188.920(1)	17 197	2459208.301(1)	17 254	2459217.828(1)	17 282	2459225.309(1)	17 304
2459190.9594(4)	17 203	2459208.641(1)	17 255	2459218.169(1)	17 283	2459225.649(1)	17 305
2459192.9995(3)	17 209	2459208.981(1)	17 256	2459218.507(1)	17 284	2459225.9884(8)	17 306
2459201.843(1)	17 235	2459209.325(1)	17 257	2459218.847(1)	17 285	2459226.3272(9)	17 307
2459202.183(1)	17 236	2459209.662(1)	17 258	2459219.187(1)	17 286	2459226.668(1)	17 308
2459202.5196(9)	17 237	2459210.004(1)	17 259	2459219.526(1)	17 287	2459227.0081(8)	17 309
2459202.863(1)	17 238	2459210.347(1)	17 260	2459219.866(1)	17 288	2459227.3490(9)	17 310
2459203.205(1)	17 239	2459210.684(1)	17 261	2459220.2058(9)	17 289	2459228.7090(4)	17 314
2459203.541(1)	17 240	2459211.026(1)	17 262	2459220.5455(9)	17 290	2459231.0903(4)	17 321
2459203.881(1)	17 241	2459211.364(1)	17 263	2459220.888(1)	17 291	2459232.7909(3)	17 326
2459204.224(1)	17 242	2459211.702(1)	17 264	2459221.226(1)	17 292	2459236.8702(3)	17 338
2459204.563(1)	17 243	2459212.043(1)	17 265	2459221.567(1)	17 293	2459293.6642(3)	17 505
2459204.901(1)	17 244	2459212.382(1)	17 266	2459221.904(1)	17 294		
2459205.242(1)	17 245	2459212.726(1)	17 267	2459222.2481(9)	17 295		

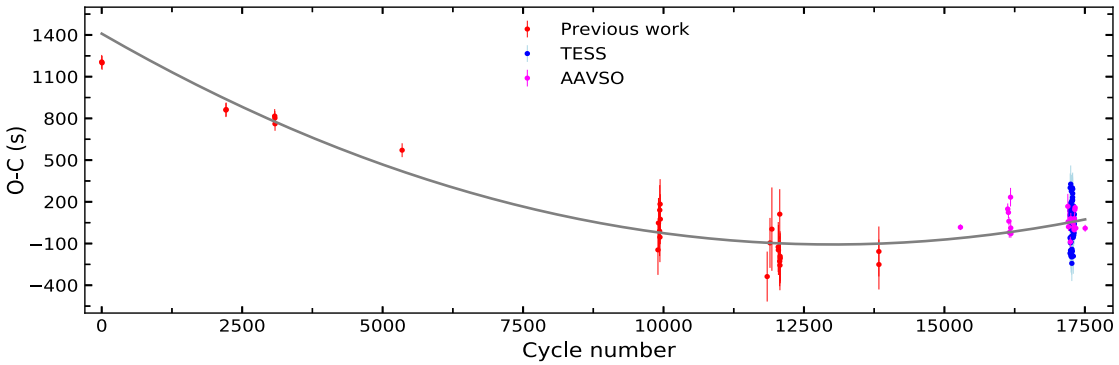

Figure 6. Observed minus calculated (O-C) diagram for the source V902 Mon. The red points are from previous work done by Witham et al. (2007), Aungwerojwit et al. (2012), and Worpel et al. (2018), whereas the blue and magenta points are from this work as observed from TESS and AAVSO, respectively.

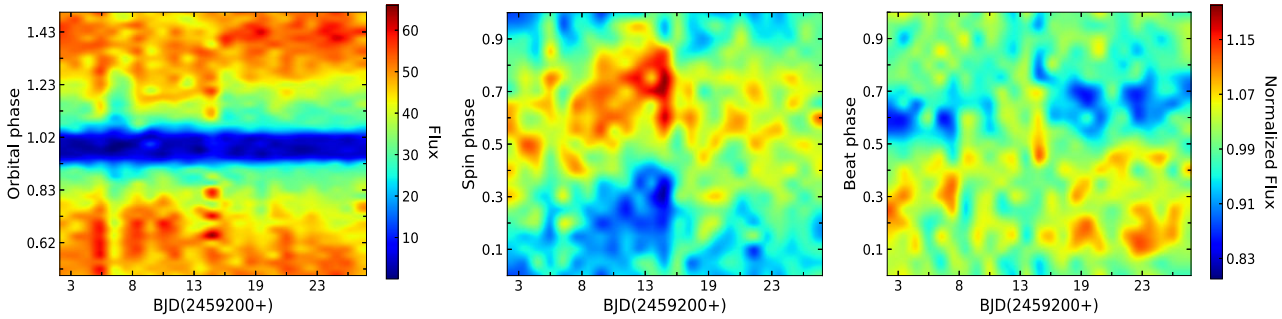

Figure 7. The **left panel** shows orbital phase-folded light curve of V902 Mon. The colourbar shows the (unnormalized) flux values. The right two panels show phase-folded light curves for spin and beat periods. The same colourbar (normalized flux) has been used for representing the spin and beat modulations.

In the case of TESS observations, we were able to identify 17 eclipse profiles clearly with nine of them round-shaped and eight of them flat-shaped. Similar to AAVSO data, TESS observations corresponding to the round-shaped and flat-shaped eclipse profile also show either presence or dominance of spin and beat frequencies, respectively. However, the power spectra corresponding to the one round-shaped and two flat-shaped eclipse profiles light curves have beat and spin frequency dominant power spectra, respectively.

We noticed that for ∼88 per cent of times when there is the presence of spin only or dominance of spin over beat, eclipses were

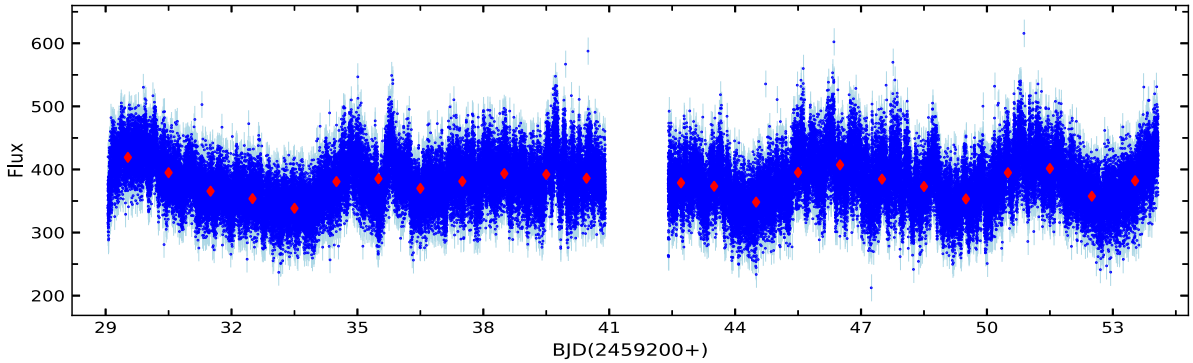

Figure 8. TESS light curve of J0746; **where** the red diamonds represent the mean flux of each day.

round in shape, whereas for ∼89 per cent of times when the beat is dominant over spin, eclipses have flat bottoms. We also suggest that the round-shaped eclipse profile corresponds to a disc-dominated accretion, whereas the flat bottom eclipse profile may correspond to the stream-dominated accretion.

5.5 Orbital inclination and eclipsed size

We have also estimated the inclination angle for V902 Mon using a similar approach of Aungwerojwit et al. (2012), which incorporates the formulae given by Eggleton (1983) with the known values of the full width of the eclipse at half-depth ($\Delta\phi_{1/2}$) and mass ratio ($q = M_2/M_1$). From the folded light curve analysis, the mean value of $\Delta\phi_{1/2}$ is determined to be ∼0.124, which is consistent with the earlier estimates of Aungwerojwit et al. (2012). Using the mean empirical mass–period relation of Smith & Dhillon (1998), M_2 falls in the range of $0.87\ M_\odot \lesssim M_2 \lesssim 0.97\ M_\odot$. We have used the mean WD mass value of $0.85 \pm 0.21\ M_\odot$ determined by Ramsay (2000) for our further calculations. The stable mass transfer from secondary to primary requires $q \lesssim 1.0$ and hence, for these values of M_1 and M_2, q can be estimated as $0.8 \lesssim q \lesssim 1.0$. This finally leads to the estimation of orbital inclination of $79.4^\circ \lesssim i \lesssim 83.0^\circ$, which is very well consistent with the earlier estimates by Aungwerojwit et al. (2012) and Worpel et al. (2018).

We have also determined the radius of the eclipsed region (R) using the following equation given by Bailey (1990):

$$R = \pi a \sqrt{(1-\alpha^2)}\, \Delta\phi_{\rm ie}, \tag{2}$$

where a is the binary separation, $\Delta\phi_{\rm ie}$ is ingress/egress duration, and $\alpha = \cos i/\cos i_{\rm lim}$, where i is the inclination angle and $i_{\rm lim}$ is the limiting angle of inclination for which eclipse half-width at half depth reaches zero. The value of $i_{\rm lim}$ depends on mass ratio q. The average value of $\Delta\phi_{\rm ie}$ for V902 Mon is derived to be 0.047 ± 0.015, where the error on $\Delta\phi_{\rm ie}$ is the standard deviation of different measurements. Considering the mean values of i and q, the radius of the eclipsed region is estimated to be $\sim 32\ R_{\rm WD}$, indicating the presence of extended emitting regions, which is also suggested by Worpel et al. (2018).

6 SWIFT J0746.3-1608

6.1 Light curve and power spectral analysis

Fig. 8 represents the TESS light curve of J0746 in which variable nature of the source is clearly evident. Due to better time resolution with 20-s cadence data, we have shown the LS power spectrum of the entire data set in Fig. 9(a). The frequencies identified in the power spectrum are Ω, 2Ω, 3Ω, 8Ω, $\omega - 2\Omega$, $\omega - \Omega$, ω, $\omega + \Omega$, $2(\omega - \Omega)$, and $2\omega - \Omega$. The periods corresponding to these frequencies are given in Table 5. The orbital period obtained from the present photometric analysis of 9.38 ± 0.04 h is consistent with the earlier reported value by Thorstensen & Halpern (2013). However, the dominant power at 2Ω in comparison to the Ω frequency suggests a strong contribution from the secondary star due to its ellipsoidal modulation. Using the longer baseline available with TESS data, we have refined the spin period as 2249.0 ± 0.6 s. The frequency corresponding to the period of 2409.5 ± 0.7 s is also present in the power spectra and can be attributed to the beat period of the system, which was not present in the earlier observations (see Bernardini et al. 2019, for details). The ω frequency was found to have slightly more power in comparison to the $\omega - \Omega$ frequency in the power spectrum indicating a disc-overflow accretion. Further, the presence of $\omega - \Omega$ seems intrinsic because if $\omega - \Omega$ would have been the orbital modulation of ω frequency, then the power at $\omega - \Omega$ and $\omega + \Omega$ should be almost same, but this is not the case for J0746 (see Fig. 9(a)). These features have also been observed by Norton et al. (1992) for FO Aqr, where they did not find equal power at both frequencies and suggested that the $\omega - \Omega$ modulation must be intrinsic to the source. Thus, we suggest the $\omega - \Omega$ modulation in the source J0746 could be originating from the accretion through the stream. We speculate that the origin of $\omega - 2\Omega$ frequency cannot be due to the modulation of ω at 2Ω; otherwise, $\omega + 2\Omega$ should also be present, which was also seen in EX Hya by Siegel et al. (1989). Therefore, we suggest that the orbital modulation of the $\omega - \Omega$ component ($\omega - \Omega \pm \Omega = \omega - 2\Omega$ and ω) might be the possible origin of $\omega - 2\Omega$, which can also alter the power at ω frequency. The $2\omega - \Omega$ frequency, which is marginally detected, can be thought of the interaction between ω and $\omega - \Omega$ frequencies because $\omega \pm \omega - \Omega = 2\omega - \Omega$ and Ω. In the asymmetric model of Wynn & King (1992) for X-ray regimes, its presence is related to stream-fed accretion for high inclination systems. However, Ferrario & Wickramasinghe (1999) have not discussed this frequency in their theoretical optical power spectral modelling. Furthermore a cluster of frequencies between 0.1 and 0.4 c/d is also present in the power spectrum with no perceivable relation to frequencies identified in J0746's power spectrum. Therefore, the presence of $\omega - \Omega$, $2(\omega - \Omega)$, ω, Ω, 2Ω, $\omega - 2\Omega$, and $2\omega - \Omega$ frequencies suggest that during TESS observations, J0746 seems to be accreting via a combination of disc and stream.

6.2 Time-resolved power spectra and phase-folded light curves

Following a similar approach as mentioned in Section 5.1 for V902 Mon, 1-d time-resolved power spectrum analysis has been done for J0746. The corresponding power spectrum is shown in Fig. 9(b). All

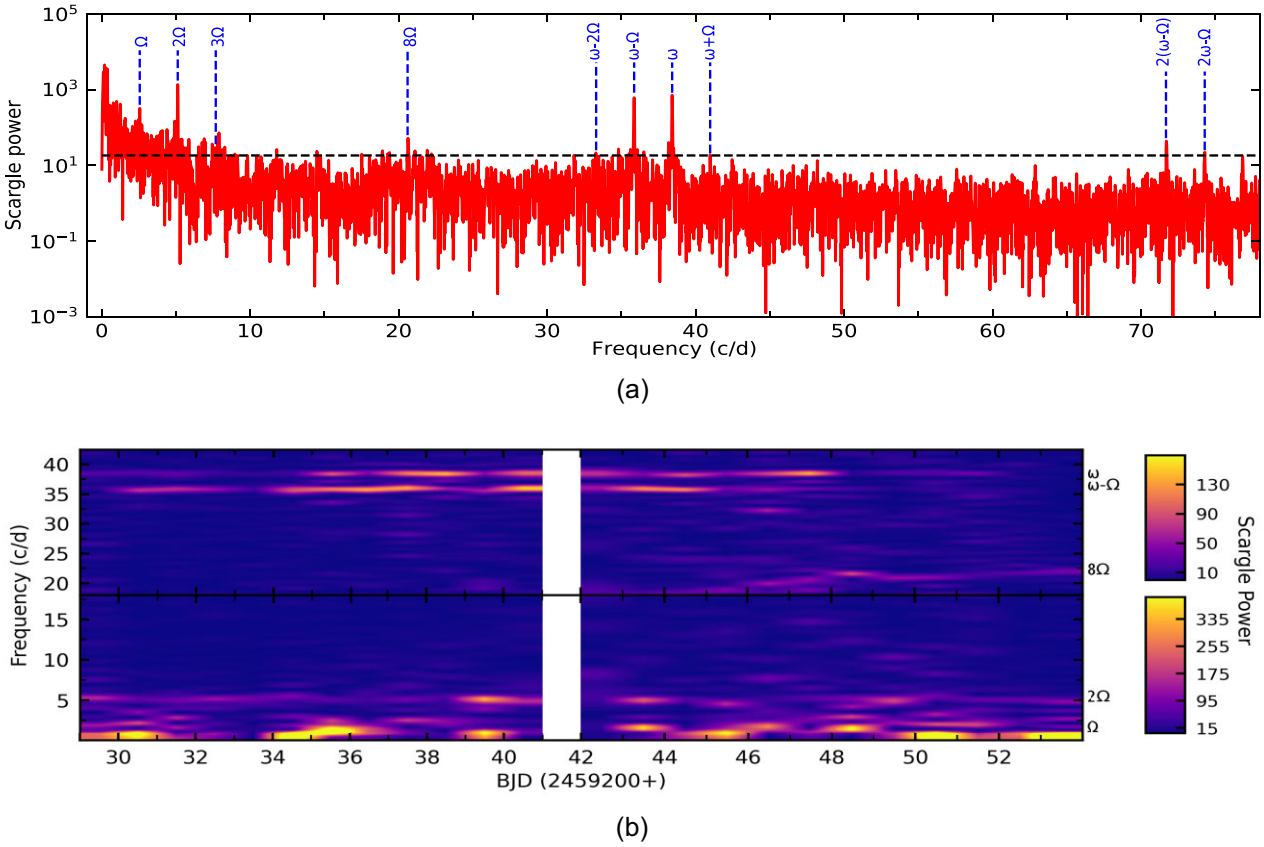

Figure 9. (a) Power spectrum of J0746 of 20 s cadence data. Major frequencies are marked for clear visual inspection. (b) Time-resolved power spectra of J0746 of 20 s cadence observations with a time-bin of 1 d.

Table 5. Periods corresponding to the dominant peaks in the power spectra of 2 min and 20 s data of J0746.

Identification	Period	
	2 min	20 s
P_{Ω} (h)	9.38 ± 0.04	9.38 ± 0.04
P_{ω} (s)	2248.8 ± 0.6	2249.0 ± 0.6
$P_{\omega-\Omega}$ (s)	2409.2 ± 0.7	2409.5 ± 0.7
$P_{2\Omega}$ (h)	4.690 ± 0.009	4.690 ± 0.009
$P_{2(\omega-\Omega)}$(s)	1204.8 ± 0.2	1204.8 ± 0.2
$P_{3\Omega}$ (h)	–	3.127 ± 0.004
$P_{8\Omega}$ (h)	–	1.1635 ± 0.0006
$P_{\omega+\Omega}$(s)	–	2108.6 ± 0.5
$P_{\omega-2\Omega}$(s)	–	2596.1 ± 0.8
$P_{2\omega-\Omega}$(s)	–	1162.9 ± 0.2

dominant frequencies Ω , 2Ω , ω - Ω , ω , and 8Ω are also marked and found to have varying powers. For 22 d, both ω and ω - Ω frequencies were present in the power spectrum with varying dominance of powers between them, suggesting a disc-overflow accretion during these days. Out of these 22 d, J0746 was found to be accreting via disc-overflow with disc-fed dominance on 9 d and disc-overflow with stream-fed dominance on 13 d. For rest 2 d, both frequencies were not found to be present in the power spectra. Further, from Day 45 to 53, 8Ω was found to be significant in the power spectrum.

The 1-d time segments data were also taken for folding over orbital, spin, and beat periods. The reference time for folding was the first point of observations. The phase-folded light curves are shown in Fig. 10. The orbital folded light curves have two maxima and two minima with a phase difference of 0.35 and 0.3, respectively. The double-humped orbital modulation seen in these orbital phase-folded light curves also suggest the ellipsoidal modulation of the secondary star. From these folded light curves, the dominance of orbital modulation over the spin and beat modulation can be easily seen. Further, the amplitude of orbital modulation was found to be varying as the observing days progress. Moreover, from Days 30 to 37, 39 to 40, 43 to 44, and 48, modulation at the beat frequency was more than the modulation at spin frequency. For Days 29, 38, 42, 45 to 47, and 49 to 51, spin modulation dominates over beat modulation. The interplay between the dominance of spin and beat modulation is also consistent with the time-resolved power spectral analysis.

Therefore, TESS observations of J0746 suggest that J0746 accretes via a combination of a disc and stream with variable dominance of both accretions. Such a change might be related to variable mass accretion rate along with the change in the activity of the secondary star, as also suggested by Bernardini et al. (2019) for J0746.

7 DISCUSSION

We have carried out detailed time-resolved timing analyses of three CVs using the high-cadence optical photometric data from TESS. From the present analyses, we speculate that LS Cam is a superhumping CV, whereas V902 Mon and J0746 belong to the IP category of MCVs.

We do not have strong evidence for pure IP classification of LS Cam, therefore we will discuss our results with an analogy of a superhumping CV. As per our knowledge, there are only 12 CVs that show simultaneous negative superhumps and superorbital periods

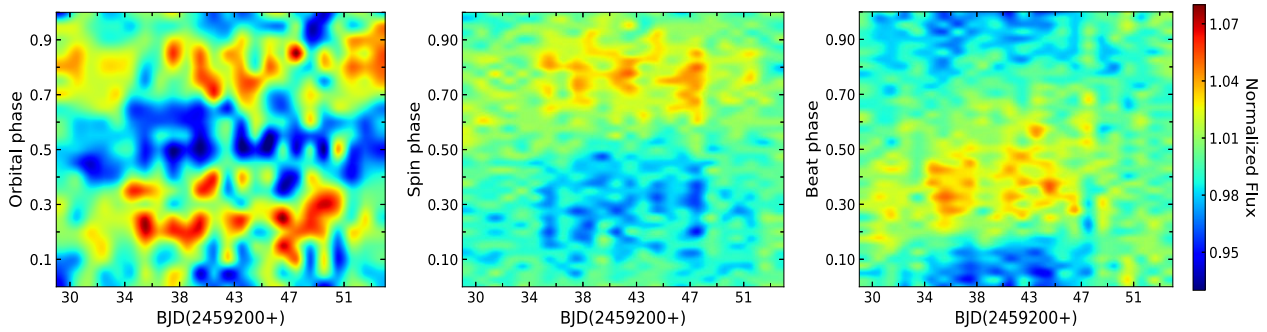

Figure 10. Phase-folded light curves of J0746 of 20 s cadence observations over orbital, spin, and beat periods. The same colourbar (normalized flux) has been used for representing the orbital, spin, and beat modulations.

(see table 5 of Armstrong et al. 2013) and if we consider LS Cam as a superhumping CV, then this number increases to 13. The negative superhump is 'permanent' as it was found to be present in all sectors; however, the positive superhump was present only in the last two sectors of observations. The simultaneous presence of positive and negative superhumps also implies that the origin of the two cannot be the same. Moreover, there are a few CVs in which both superhumps have been simultaneously detected, e.g. V503 Cyg (Harvey et al. 1995), V603 Aql (Patterson et al. 1997), AM CVn (Harvey et al. 1998), V442 Oph (Patterson et al. 2002), TT Ari (Belova et al. 2013), and AQ Men (Iłkiewicz et al. 2021). Therefore, LS Cam is an important addition to this group. The most accepted model in CVs and LMXBs to explain the simultaneous presence of superorbital period and negative superhump is the wobbling-disc model, where lines of nodes of the accretion disc precess retrogradely. This causes a negative superhump period to arise due to the interaction between precession and orbital motions. The presence of ω_0 + N frequency along with N frequency could be a result of the changing of the visible disc area with the wobble frequency N (Patterson et al. 2002). Although the origin of a tilted disc in LMXBs is known, we do not have a clear picture for CVs. Further, a positive superhump arises due to the beating between the orbital and the prograde precession period of the elliptic accretion disc. The disc becomes elliptic because of the tidal instability which is produced due to the 3:1 tidal resonance in an accretion disc (Whitehurst 1988; Osaki 1989; Lubow 1991). The permanent negative superhumps have been commonly found in other kinds of CVs such as SW Sex stars, VY Scl stars, and novalike variables. Therefore, extensive X-ray and optical spectroscopic observations are required to explore the true nature of LS Cam.

IPs are generally clustered into three groups: the slow rotators with $P_\omega/P_\Omega \sim 0.5$, intermediate with $P_\omega/P_\Omega \sim 0.1$, and fast with $P_\omega/P_\Omega \sim 0.01$. With $P_\omega/P_\Omega \sim 0.08$ and 0.07 respectively, for V902 Mon and J0746 both fall in the category of intermediate rotators, where the majority of the IPs generally lie (Norton, Somerscales & Wynn 2004; Bernardini et al. 2017). V902 Mon and J0746 are long orbital period systems and therefore both are interesting from an evolutionary perspective. V902 Mon was identified as a likely disc-accreting IP by Worpel et al. (2018) due to the absence of ω - Ω frequency in the power spectrum, whereas J0746 was identified as a possible IP by Bernardini et al. (2019) and it was also found to be changing between low and high states (Bernardini et al. 2017, 2019). It has shown the fastest state transition in X-rays within less than a day. The detection of ω - Ω frequency for the first time along with ω frequency in the combined power spectra obtained from TESS indicate that V902 Mon and J0746 accrete via a combination of disc and stream. However, 1-d time-resolved power spectra show us a bigger picture, where the power spectra seem to be changing on a time-scale of days. Among disc-overflow systems, there are two IPs, FO Aqr and TX Col, which have been observed and studied several times. Moreover, the change in the accretion mechanism based on the presence of spin and beat frequency in the power spectra of these IPs has been previously explored by many authors (see Buckley & Tuohy 1989; Beardmore et al. 1996; Norton et al. 1997; Littlefield et al. 2020; Rawat et al. 2021, for details). This indicates that maybe this type of behaviour is the true nature of these systems and due to observational constraints, we were not able to detect this for the majority of IPs. Therefore, an extensive study with a larger sample is needed to connect a bridge between varying powers in the power spectra and accretion mechanism.

8 SUMMARY

We summarized our findings as follows:

(i) A periodicity of ∼4 d along with another periodicity of 3.301 h for LS Cam in all sectors of the TESS observations is found to be present and can be attributed to the superorbital and negative superhump periods, respectively. The simultaneous presence of both periods suggests a wobbling disc model for its origin. A positive superhump period of ∼3.7 h was also found to be present in the observations of the last two sectors, which could be due to the prograde precession period of the elliptic accretion disc. The values of period excess and period deficit were found to be 0.0875(35) and −0.03406(6), respectively. The mass ratio of the binary system components is found to be 0.321(6).

(ii) We have detected a beat period of 2387.0(6) s for the first time in V902 Mon. Our results presented in this study hint towards the change in accretion mode during the entire period of the observation, where disc-fed dominated accretion was found to be taking place for the majority of the time. We have refined the previously confirmed spin period with a value of 2207.6(5) s as well as orbital ephemeris. Moreover, we have also found an apparent orbital period derivative of $(6.09 \pm 0.60) \times 10^{-10}$. Further, we have shown that eclipsed region indicates the presence of extended emitting regions.

(iii) In the case of J0746, a beat period of 2409.5(7) s is obtained, which was not evident in earlier studies. Moreover, using TESS observations, we were able to refine the previously reported spin period as 2249.0(6) s. Our results suggest variable accretion mechanisms taking place during the entire observation period. For more than half of the observing time, J0746 was found to be stream-fed dominant accretor. The dominant modulation at 2Ω seems to be due to the ellipsoidal modulation of the secondary star.

ACKNOWLEDGEMENTS

We thank the anonymous referee for providing useful comments and suggestions that led to the significant improvement of the quality of the paper. This paper includes data collected with the TESS mission, obtained from the MAST data archive at the Space Telescope Science Institute (STScI). Funding for the TESS mission is provided by the NASA Explorer Program. Based on observations obtained with the Samuel Oschin 48-inch and the 60-inch Telescope at the Palomar Observatory as part of the Zwicky Transient Facility project. ZTF is supported by the National Science Foundation under Grant No. AST-1440341 and AST-2034437 and a collaboration including Caltech, IPAC, the Weizmann Institute for Science, the Oskar Klein Center at Stockholm University, the University of Maryland, the University of Washington, Deutsches Elektronen-Synchrotron and Humboldt University, Los Alamos National Laboratories, the TANGO Consortium of Taiwan, the University of Wisconsin at Milwaukee, Trinity College Dublin, Lawrence Livermore National Laboratories, Lawrence Berkeley National Laboratories, and IN2P3, France. Operations are conducted by COO, IPAC, and UW. We acknowledge with thanks the variable star observations from the AAVSO International Database contributed by observers worldwide and used in this research. NR acknowledges Mr. Prajjwal Rawat and Mr. Jaydeep Singh for technical discussion.

DATA AVAILABILITY

The data sets were derived from the TESS data archive available at https://archive.stsci.edu/missions-and-data/tess. The data underlying this article will be shared on reasonable request to the corresponding author.

REFERENCES

Armitage P. J., Livio M., 1996, ApJ, 470, 1024
Armstrong E. et al., 2013, MNRAS, 435, 707
Aungwerojwit A., Gänsicke B. T., Wheatley P. J., Pyrzas S., Staels B., Krajci T., Rodríguez-Gil P., 2012, ApJ, 758, 79
Bailey J., 1990, MNRAS, 243, 57
Beardmore A. P., Mukai K., Norton A. J., Osborne J. P., Taylor P., 1996, in Zimmermann H. U., Trümper J., Yorke H., eds, Roentgenstrahlung from the Universe. International Conference on X-ray Astronomy and Astrophysics, p. 123
Bellm Eric C. (Jan 2019) The Zwicky Transient Facility: System Overview, Performance, and First Results Publications of the Astronomical Society of the Pacific, Volume 131, Issue 995, pp. 018002 (2019).
Belova A. I., Suleimanov V. F., Bikmaev I. F., Khamitov I. M., Zhukov G. V., Senio D. S., Belov I. Y., Sakhibullin N. A., 2013, Astron. Lett., 39, 111
Bernardini F., de Martino D., Mukai K., Falanga M., 2019, MNRAS, 484, 101
Bernardini F., de Martino D., Mukai K., Russell D. M., Falanga M., Masetti N., Ferrigno C., Israel G., 2017, MNRAS, 470, 4815
Buckley D. A. H., Tuohy I. R., 1989, ApJ, 344, 376
Dobrzycka D., Dobrzycki A., Engels D., Hagen H.-J., 1998, AJ, 115, 1634
Eastman J., Siverd R., Gaudi B. S., 2010, PASP, 122, 935
Eggleton P. P., 1983, ApJ, 268, 368
Fausnaugh M. M. et al., 2021, ApJ, 908, 51
Ferrario L., Wickramasinghe D. T., 1999, MNRAS, 309, 517
Gaia Collaboration, 2021, A&A, 650, C3
Hameury J. M., King A. R., Lasota J. P., 1986, MNRAS, 218, 695
Harvey D. A., Skillman D. R., Kemp J., Patterson J., Vanmunster T., Fried R. E., Retter A., 1998, ApJ, 493, L105
Harvey D., Skillman D. R., Patterson J., Ringwald F. A., 1995, PASP, 107, 551
Hellier C., 1991, MNRAS, 251, 693
Hellier C., 1993, MNRAS, 265, L35
Hellier C., Mason K. O., Smale A. P., Corbet R. H. D., O'Donoghue D., Barrett P. E., Warner B., 1989, MNRAS, 238, 1107
Horne J. H., Baliunas S. L., 1986, ApJ, 302, 757
Iłkiewicz K. et al., 2021, MNRAS, 503, 4050
Kafka S., 2021, Observations from the AAVSO International Database. Available at: https://www.aavso.org
Kato T., 2022, preprint (arXiv:2201.02945)
Kim Y., Beuermann K., 1995, A&A, 298, 165
King A. R., Lasota J.-P., 1991, ApJ, 378, 674
Littlefield C. et al., 2020, ApJ, 896, 116
Littlefield C., Scaringi S., Garnavich P., Szkody P., Kennedy M. R., Iłkiewicz K., Mason P. A., 2021, AJ, 162, 49
Lomb N. R., 1976, Ap&SS, 39, 447
Lubow S. H., 1989, ApJ, 340, 1064
Lubow S. H., 1991, ApJ, 381, 268
Murray J. R., Chakrabarty D., Wynn G. A., Kramer L., 2002, MNRAS, 335, 247
Norton A. J., Beardmore A. P., Taylor P., 1996, MNRAS, 280, 937
Norton A. J., Hellier C., Beardmore A. P., Wheatley P. J., Osborne J. P., Taylor P., 1997, MNRAS, 289, 362
Norton A. J., Somerscales R. V., Wynn G. A., 2004, in Vrielmann S., Cropper M., eds, ASP Conf. Ser. Vol. 315, Magnetic Cataclysmic Variables. Astron. Soc. Pac., San Francisco, p. 216
Norton A. J., Watson M. G., King A. R., Lehto H. J., McHardy I. M., 1992, MNRAS, 254, 705
Osaki Y., 1989, PASJ, 41, 1005
Patterson J. et al., 1997, PASP, 109, 1100
Patterson J. et al., 2002, PASP, 114, 1364
Patterson J. et al., 2005, PASP, 117, 1204
Ramsay G., 2000, MNRAS, 314, 403
Rawat N., Pandey J. C., Joshi A., 2021, ApJ, 912, 78
Retter A., Chou Y., Bedding T. R., Naylor T., 2002, MNRAS, 330, L37
Ricker G. R. et al., 2015, J. Astron. Telesc. Instrum. Syst., 1, 014003
Robertson J. W., Honeycutt R. K., Turner G. W., 1995, PASP, 107, 443
Rosen S. R., Mason K. O., Cordova F. A., 1988, MNRAS, 231, 549
Scargle J. D., 1982, ApJ, 263, 835
Scaringi S. et al., 2010, MNRAS, 401, 2207
Siegel N., Reinsch K., Beuermann K., van der Woerd H., Wolff E., 1989, A&A, 225, 97
Smith D. A., Dhillon V. S., 1998, MNRAS, 301, 767
Thorstensen J. R., Halpern J., 2013, AJ, 146, 107
Thorstensen J. R., Ringwald F. A., Taylor C. J., Sheets H. A., Peters C. S., Skinner J. N., Alper E. H., Weil K. E., 2017, Res. Notes Am. Astron. Soc., 1, 29
Vanderspek R., Doty J. P., Fausnaugh M., Villaseñor J. M. S., Jenkins J. M., Berta-Thompson Z. K., Burke C. J., Ricker G. R., 2018, TESS Instrument Handbook, Tech. rep., Kavli Institute for Astrophysics and Space Science, Massachusetts Institute of Technology
Warner B., 1986, MNRAS, 219, 347
Warner B., Cropper M., 1984, MNRAS, 206, 261
Wheatley P. J., 1999, in Hellier C., Mukai K., eds, ASP Conf. Ser. Vol. 157, Annapolis Workshop on Magnetic Cataclysmic Variables. Astron. Soc. Pac., San Francisco, p. 47
Whitehurst R., 1988, MNRAS, 232, 35
Witham A. R. et al., 2007, MNRAS, 382, 1158
Wood M. A., Montgomery M. M., Simpson J. C., 2000, ApJ, 535, L39
Worpel H., Schwope A. D., Traulsen I., Mukai K., Ok S., 2018, A&A, 617, A52
Wynn G. A., King A. R., 1992, MNRAS, 255, 83

This paper has been typeset from a TEX/LATEX file prepared by the author.